The response of a baroclinic anticyclonic eddy to relative wind stress forcing

Article

Published Version

It is advisable to refer to the publisher's version if you intend to cite from the work. See Guidance on citing.

To link to this article DOI: http://dx.doi.org/10.1175/JPO-D-22-0044.1

Publisher: American Meteorological Society

www.reading.ac.uk/centaur

CentAUR

Central Archive at the University of Reading

Reading's research outputs online

⮂The Response of a Baroclinic Anticyclonic Eddy to Relative Wind Stress Forcing

Thomas Wilder,[a] Xiaoming Zhai,[a] David Munday,[b] and Manoj Joshi[a]

[a] *School of Environmental Sciences, University of East Anglia, Norwich, United Kingdom*
[b] *British Antarctic Survey, Cambridge, United Kingdom*

ABSTRACT: Including the ocean surface current in the calculation of wind stress is known to damp mesoscale eddies through a negative wind power input and have potential ramifications for eddy longevity. Here, we study the spindown of a baroclinic anticyclonic eddy subject to absolute (no ocean surface current) and relative (including ocean surface current) wind stress forcing by employing an idealized high-resolution numerical model. Results from this study demonstrate that relative wind stress dissipates surface mean kinetic energy (MKE) and also generates additional vertical motions throughout the whole water column via Ekman pumping. Wind stress curl–induced Ekman pumping generates additional baroclinic conversion (mean potential to mean kinetic energy) that is found to offset the damping of surface MKE by increasing deep MKE. A scaling analysis of relative wind stress–induced baroclinic conversion and relative wind stress damping confirms these numerical findings, showing that additional energy conversion counteracts relative wind stress damping. What is more, wind stress curl–induced Ekman pumping is found to modify surface potential vorticity gradients that lead to an earlier destabilization of the eddy. Therefore, the onset of eddy instabilities and eventual eddy decay takes place on a shorter time scale in the simulation with relative wind stress.

KEYWORDS: Eddies; Ekman pumping/transport; Instability; Wind stress; Air-sea interaction; Energy budget/balance

1. Introduction

Baroclinic mesoscale eddies exist across much of the ocean and evolve on time scales of months to years (Chelton et al. 2011). Anticyclonic (cyclonic) eddies are categorized as having positive (negative) sea level and temperature anomalies that typically display depressed (raised) isopycnal surfaces. Eddies are energetic features that dominate the ocean's kinetic energy budget (Ferrari and Wunsch 2009), making them efficient at redistributing oceanic properties (Zhang et al. 2014; Thompson et al. 2014). Interactions between atmospheric winds and mesoscale eddies have important consequences for ocean dynamics, and as such have been the focus of numerous studies (Gaube et al. 2013; Xu et al. 2016; Oerder et al. 2018; Song et al. 2020).

The dissipation of eddies has been attributed to a handful of mechanisms, ranging from bottom drag (Arbic and Scott 2008), internal lee waves (Clément et al. 2016), western boundary graveyard effects (Zhai et al. 2010), and ocean current–wind interaction, known herein as "relative wind stress" (Duhaut and Straub 2006; Zhai and Greatbatch 2007; Zhai et al. 2012). Relative wind stress takes into account the relative motion between surface winds and ocean currents. It is parameterized by

$$\boldsymbol{\tau}_{\text{rel}} = \rho_a C_d |\mathbf{u}_a - \mathbf{u}_s|(\mathbf{u}_a - \mathbf{u}_s), \qquad (1)$$

where ρ_a is air density, C_d is a drag coefficient that is a function of wind speed, $\mathbf{u}_a$ is the atmospheric wind 10 m above the

ocean surface, and $\mathbf{u}_s$ is the ocean surface current. Neglecting $\mathbf{u}_s$ in Eq. (1) gives

$$\boldsymbol{\tau}_{\text{abs}} = \rho_a C_d |\mathbf{u}_a|\mathbf{u}_a, \qquad (2)$$

which is "absolute wind stress." Throughout, subscripts "abs" and "rel" imply absolute and relative, respectively. The total wind power input into the geostrophic circulation can be computed as

$$P = \int_S \boldsymbol{\tau} \cdot \mathbf{u}_{\text{gs}} \, dS, \qquad (3)$$

where $\boldsymbol{\tau} \cdot \mathbf{u}_{\text{gs}}$ is defined as work done by winds on the geostrophic ocean surface, $\int_S$ is the integral over horizontal space, and the subscript "gs" denotes geostrophic surface motion. Total wind power input P has units of kg m^2 s^{-3}.

Relative wind stress acts to reduce the total wind power input into large-scale geostrophic motions by ~20%–35%, ultimately slowing down the ocean circulation (Duhaut and Straub 2006; Hughes and Wilson 2008). Relative wind stress is also found to reduce mesoscale eddy kinetic energy by ~30% (Seo et al. 2016; Renault et al. 2016b; Oerder et al. 2018). The damping mechanism is illustrated in Fig. 1 for a circular anticyclonic eddy in geostrophic balance. As a surface wind blows over the eddy, the wind stress becomes modified by the eddy current, producing a larger (smaller) wind stress at the southern (northern) side of the eddy compared when the eddy current is not considered. Because the wind stress is largest at the southern side and opposes the eddy current,
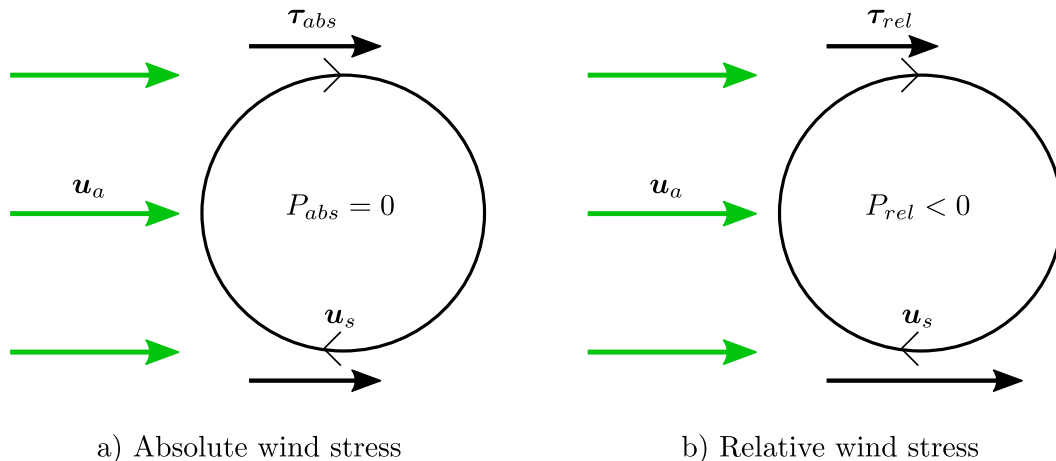
FIG. 1. Schematic depicting changes in wind stress (τ) and wind power input (P) over an isolated anticyclonic eddy. A wind that blows west to east over an eddy will produce a wind stress that generates positive and negative wind work at its northern and southern sides. (a) For an absolute wind stress, τ_{abs} is constant over the eddy, meaning there are equal amounts of positive and negative wind work at each north and south side of the eddy. A sum of total wind work over this eddy gives zero wind power input and no eddy damping. (b) Relative wind stress gives more wind stress on the southern side and less on the northern side. The asymmetry in the wind stress produces more negative than positive wind work. Summing over the whole space gives a net negative wind power input, and energy is systematically removed from the eddy.

there is more negative wind work than positive. When wind work is integrated over space, total wind power input is negative and energy is removed from the eddy. The result is the same for a geostrophically balanced cyclonic eddy, as the eddy circulation is merely directed in an anticlockwise manner, rather than clockwise.

Relative wind stress damping has other important effects on ocean processes. Through a reduction in ocean current speeds by relative wind stress, numerical simulations displayed improvements in their representation of equatorial currents (Pacanowski 1987) and western boundary current systems (Ma et al. 2016; Renault et al. 2016a). Without this damping mechanism, however, eddy features in the Agulhas Current are poorly characterized (McClean et al. 2011) and total heat transport in the Southern Ocean is overestimated (Munday et al. 2021).

A further dynamical response of relative wind stress is the production of vertical motions via Ekman pumping, which is found to attenuate eddies by flattening their isopycnals (Dewar and Flierl 1987). However, relative wind stress–induced Ekman pumping could be a potential route for the supply of energy through baroclinic conversion (Renault et al. 2018). Shan et al. (2020) show that the conversion of potential into kinetic energy could partially compensate the damping of kinetic energy by relative wind stress. In addition, Ekman pumping due to relative wind stress is also known to play an important role in the supply of nutrients from the deep ocean into the euphotic zone (McGillicuddy et al. 2007; Gaube et al. 2014).

The structure of eddies can also impact their lifetime. For example, the stability of monopole baroclinic eddies is found to decrease with an increase in baroclinic shear, leading to a breakup of the initial vortex structure (Ikeda 1981). Eddies

with strong baroclinic components typically exhibit a deep flow that is counter to its surface rotation, destabilizing baroclinic eddies (Dewar and Killworth 1995). In this counterrotating setup, upper- and lower-layer potential vorticity gradients oppose each other, providing a necessary condition for baroclinic instability (Pierrehumbert and Swanson 1995). Dewar et al. (1999) found that eddy stability can be enhanced by a stronger barotropic component, a deep corotating flow, implying a reduction of opposing potential vorticity gradients between upper and lower layers. In a linear stability analysis, Katsman et al. (2003) reveal growth rates of the most unstable azimuthal modes are drastically reduced when the vertical eddy structure transitioned from counter to corotating.

This paper aims to examine the role that relative wind stress has on a baroclinic anticyclonic eddy. First, when the eddy is subject to relative wind stress and its associated negative wind power input, does this lead to a complete eddy spindown? Second, can Ekman pumping generate additional kinetic energy through baroclinic conversion that offsets relative wind stress damping? Finally, how might the stability of a baroclinic counterrotating eddy be affected by relative wind stress? In section 2, descriptions of the model setup and key theoretical techniques are given. In section 3, we present our main findings, showing how the eddy responds to each wind stress formula. In section 4, we summarize and discuss the results.

2. Methods

a. Experimental setup

The MIT general circulation model (Marshall et al. 1997) is employed in this study. The model is set in an idealized configuration, whereby a single eddy is allowed to evolve in a

TABLE 1. Key model parameters.

Symbol	Value	Description
$L_{x,y}$	2000 km	Domain size
H	4000 m	Ocean depth
H_1	800 m	Upper-layer ocean depth
$\Delta x, y$	10 km	Horizontal grid resolution
Δz	5–100 m	Vertical grid spacing
f	9.3461×10^{-5} s^{-1}	Coriolis frequency
A	25 cm	Eddy amplitude
R	100 km	Eddy e-folding radius
$\mathbf{u}_a$	7 m s^{-1}	Wind speed
T'	2.5°C	Temperature anomaly
γ, B	1, 3	Governs stratification
ρ_0	1026 kg m^{-3}	Reference ocean density
$\Delta\rho$	3 kg m^{-3}	Density difference between layers
N_0	10^{-5} s^{-1}	Reference buoyancy frequency
A_4	8×10^{10} m^4 s^{-1}	Biharmonic viscous coefficient
A_z	1×10^{-4} m^2 s^{-1}	Vertical viscous coefficient
κ_4	3.2×10^9 m^4 s^{-1}	Biharmonic diffusive coefficient
κ_z	4×10^{-5} m^2 s^{-1}	Vertical diffusive coefficient

box-like domain while being forced by a surface wind stress. The idealized approach allows the underlying physics of eddy–wind interactions to be diagnosed.

The eddy sits on an f plane at a latitude of 40°N and the domain spans 2000 km in each horizontal direction with mesoscale resolving resolution of 10 km. In the vertical, the domain is 4000 m deep and has 91 z levels with grid spacing of 5 m at the surface and 100 m near the bottom. Generated using Stewart et al. (2017), this vertical grid is designed to ensure that baroclinic modes are correctly resolved in z-coordinate ocean models. At the boundary edges the flow is reentrant, meaning what leaves the north (east) boundary reenters through the south (west), and vice versa. A temperature sponge layer of width 100 km is applied at each boundary edge and is restored daily, making sure that any temperature signals propagated from the eddy do not cross the boundary edge and reenter the domain. At the bottom boundary, a free-slip condition is used along with zero bottom drag. Values of key parameters can be found in Table 1.

At the grid scale, energy dissipation and temperature diffusion are parameterized using biharmonic operators. The Prather advection scheme (Prather 1986) is used in the temperature equation to preserve any sharp frontal structures that might arise in the flow. Moreover, the use of the Prather scheme has been found to reduce levels of spurious diapycnal mixing in high-resolution z-coordinate models (Hill et al. 2012). In the vertical, constant viscous and diffusive coefficients are employed, as well as convective adjustment to remove static instability.

Initial eddy conditions are derived from a thermal wind balance and employ a Gaussian function for its sea surface height and horizontal temperature profile (Chelton et al. 2011). The sea surface height is given by

$$\eta(x,y) = A\exp[-(x^2 + y^2)/R^2], \tag{4}$$

where A is the eddy sea surface amplitude and R is the e-folding radius, which is the point of zero vorticity. Maximum geostrophic velocities occur at $L_s = 2^{-1/2}R$, the speed-based radius (Chelton et al. 2011). The temperature profile is

$$T(x,y,z) = T'\exp[-(x^2 + y^2)/R^2]\exp[-\gamma(z/H_1)] + T_{ref}(z), \tag{5}$$

where T' is the temperature anomaly, γ governs the stratification of the water column, and H_1 is the effective thermocline depth. Figure 2a shows a transect of this temperature profile. The use of γ in Eq. (5) produces a temperature profile that decays with depth, necessary to generate a counterrotating lower layer. The reference background temperature profile, $T_{ref}(z)$, is found using the linear equation of state, where the reference background density profile is given by

$$\rho_{ref}(z) = \rho_0[1 - N_0^2(z/g)] + 0.5\Delta\rho\{1 - \tanh[B(z + H_1)/H]\}, \tag{6}$$

where ρ_0 is a reference density, N_0 is a reference buoyancy frequency, g is the gravitational constant, z are vertical grid levels, $\Delta\rho$ is the difference in density between the surface and bottom, B is the gradient of the density profile, and H is the depth of the ocean.
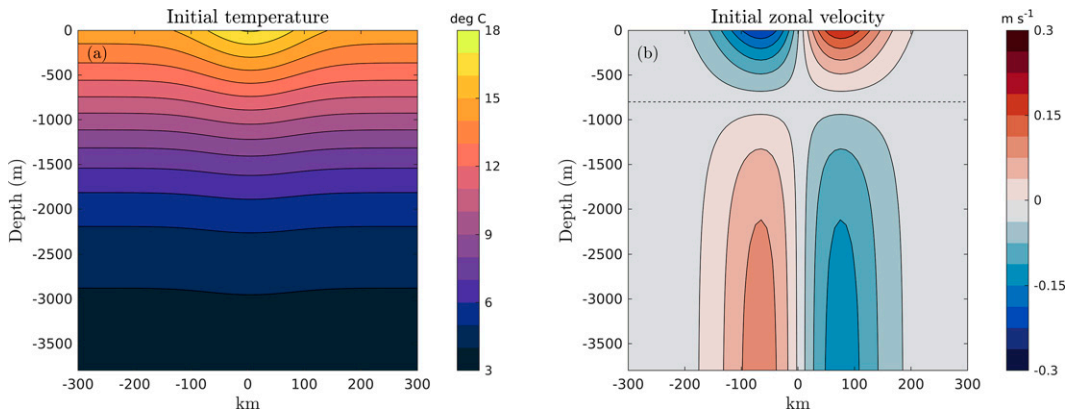

FIG. 2. Meridional transects through the eddy center of (a) initial temperature (°C) and (b) zonal velocity (m s^{-1}). The horizontal dashed line in (b) is the depth of the upper layer, $H_1 = 800$ m.

Horizontal velocity components of the eddy are in geostrophic balance

$$\mathbf{u}_g(x,y,z) = \frac{g}{f}\,\mathbf{k}\times\left[\nabla\eta + \alpha\int_z^0 \nabla T\,dz\right], \tag{7}$$

where f is the Coriolis frequency, α is the thermal expansion coefficient, and $\mathbf{u}_g = (u_g, v_g)$ are zonal and meridional geostrophic velocity components. The subscript g symbolizes geostrophic components. The first term in the square brackets is the surface velocity derived from the Gaussian sea surface height, and the second term is the vertical shear derived through thermal wind balance. Figure 2b displays a transect of initial velocity, with the counterrotating setup clearly visible.

The wind setup follows McGillicuddy (2015). A spatially uniform background wind begins in the west to east direction and rotates $2\pi/64$ every hour, meaning the wind vectors make one full rotation every 64 h. Choosing this rotation period avoids inertial disturbances developing in the eddy shape, and also minimizes Ekman transport that could lead to sea level height discontinuities at the boundary edges.

In this analysis, two main simulations are carried out: absolute wind stress (AW) and relative wind stress (RW). An additional simulation with no-wind forcing is run as our control experiment and shows how the eddy evolves on its own. Prior to any analysis, a 10-day model adjustment phase is run to allow any waves to die down. After this adjustment, the wind is turned on immediately and each simulation is run for 400 days in total.

b. Ekman pumping

Total Ekman pumping is defined following Stern (1965):

$$W_{\text{tot}} = \frac{1}{\rho_0}\,\mathbf{k}\cdot\nabla\times\left[\frac{\boldsymbol{\tau}}{(f+\zeta_g)}\right], \tag{8}$$

$$= \underbrace{\frac{\mathbf{k}\cdot\nabla\times\boldsymbol{\tau}}{\rho_0(f+\zeta_g)}}_{W_c} + \underbrace{\frac{1}{\rho_0(f+\zeta_g)^2}\left(\tau^x\frac{\partial\zeta_g}{\partial y} - \tau^y\frac{\partial\zeta_g}{\partial x}\right)}_{W_\zeta}, \tag{9}$$

where ζ_g is the geostrophic relative vorticity, and τ^x and τ^y are zonal and meridional wind stress components, respectively. The W_{tot} is calculated using daily time-mean quantities, as is the case for all terms except energetics in section 2c.

Total Ekman pumping W_{tot} consists of two components: linear Ekman pumping W_c—induced by a wind stress curl—and nonlinear Ekman pumping W_ζ—induced by vorticity gradients. For a uniform background wind, relative wind stress generates a wind stress curl because of its spatial variability over the eddy, whereas absolute wind stress is constant everywhere and no gradients in wind stress will exist (see Fig. 1). Therefore, only relative wind stress induces linear Ekman pumping, which produces upwelling at the center of anticyclonic eddies, enabling spindown through a flattening of isopycnals (Dewar and Flierl 1987). On the other hand, nonlinear Ekman pumping takes place irrespective of the wind stress formula, and will exhibit dipoles of up/downwelling.

The primary effect of W_ζ is to advect the eddy by tilting isopycnals (Stern 1965). Similarly to Gaube et al. (2015), we expect W_c to be the dominant attenuation process in this eddy setup.

c. Energetics

To understand the eddy spindown process, we make use of the quasigeostrophic energetic framework defined by von Storch et al. (2012). In the following definitions, the time mean refers to a 16-day rolling average, and turbulent terms are perturbations from this mean. The choice of this 16-day time mean is made to avoid aliasing any unwanted signal that might come from averaging a noninteger multiple of wind rotations, i.e., 16 days works out at 6 full wind rotations. Mean energy terms help diagnose the total evolution of the eddy, and are denoted by subscript M. Turbulent energy terms are useful to examine eddy instability pathways, and are denoted by subscript T. Conversions between energy reservoirs are symbolized by $C(X,Y)$. For $C(X,Y) > 0$, X is converted to Y, and $C(X,Y) < 0$, Y is converted to X.

Mean potential and mean kinetic energy are described using

$$\text{PE}_M = -\int_V \frac{g}{2n_0}\,\overline{\rho^*(x,y,z,t)}^2\,dV, \quad\text{and} \tag{10}$$

$$\text{KE}_M = \int_V \frac{\rho_0}{2}(\overline{u}_g^2 + \overline{v}_g^2)\,dV, \tag{11}$$

where the overbar represents a time mean, $\rho^*(x,y,z,t) = \rho(x,y,z,t) - \rho_{\text{ref}}(z)$ is a density anomaly relative to a constant-in-time reference background density state, n_0 is the vertical gradient of $\rho_{\text{ref}}(z)$, from Eq. (6), and $\int_V$ is the volume integral. Both PE_M and KE_M have units of kg m^2 s^{-2}. This quasigeostrophic framework has been employed in previous energy analyses (Chen et al. 2014; Youngs et al. 2017).

The mean kinetic energy describes the strength of the eddy flow, and its temporal evolution is governed by energy conversions, wind work, and viscous dissipation:

$$\frac{\partial\text{KE}_M}{\partial t} = C(\text{PE}_M, \text{KE}_M) + P + \epsilon(\text{KE}_M), \tag{12}$$

where

$$C(\text{PE}_M, \text{KE}_M) = -\int_V g\overline{\rho}\,\overline{w}\,dV, \quad\text{and} \tag{13}$$

$$P = \int_S \overline{\boldsymbol{\tau}}\cdot\overline{\mathbf{u}}_{\text{gs}}\,dS. \tag{14}$$

In Eq. (12), divergence and advection terms have been neglected because they do not contribute to the time evolution of domain-integrated KE_M. Equation (13) describes the conversion between PE_M and KE_M, and has units of kg m^2 s^{-3}. When $C(\text{PE}_M, \text{KE}_M) > 0$, PE_M is transferred to KE_M, and this can be thought of as baroclinic conversion. This term is governed by fluxes of density up and down the water column and may be an important term because it could be affected by
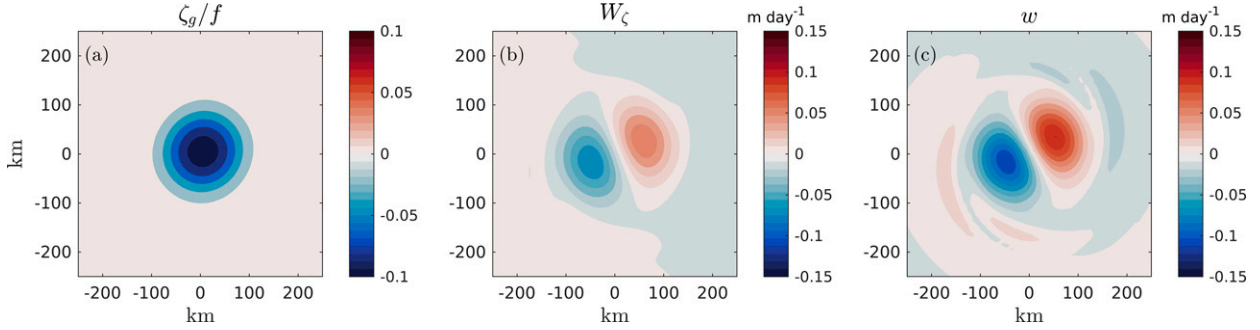
FIG. 3. Horizontal patterns at day 100 in absolute wind stress simulation of (a) surface normalized relative vorticity, (b) nonlinear Ekman pumping (m day^{-1}), and (c) model output vertical velocity (m day^{-1}) at a depth of 5 m. Quantities are calculated using MITgcm daily time-mean output.

relative wind stress–induced Ekman pumping. Equation (14) is wind power input, also shown in Eq. (3). In the case of a uniform background wind and relative wind stress, P will dissipate mesoscale eddies (Xu et al. 2016). The last term $\epsilon(\text{KE}_M)$ is made up of turbulent momentum transfers and viscous processes.

Diagnosing turbulent eddy terms can inform on the presence of eddy instabilities. Turbulent kinetic energy is

$$\text{KE}_T = \int_V \frac{\rho_0}{2} \overline{(u_g'^2 + v_g'^2)} \, dV, \tag{15}$$

where the primes are fluctuations from their time-mean. KE_T has units of kg m^2 s^{-2}. Conversion terms that transfer turbulent energy in and out of KE_T are given by

$$C(\text{KE}_T, \text{KE}_M) = \int_V (\rho_0 \overline{u_g' \mathbf{u}'} \cdot \nabla \overline{u}_g + \rho_0 \overline{v_g' \mathbf{u}'} \cdot \nabla \overline{v}_g) \, dV, \tag{16}$$

$$C(\text{PE}_T, \text{KE}_T) = -\int_V g \overline{\rho' w'} \, dV, \tag{17}$$

where $\mathbf{u} = (u_g, v_g, w)$. Equation (16) is the conversion between turbulent kinetic energy and mean kinetic energy by momentum fluxes. This is the barotropic pathway and barotropic instability takes place when shear in the mean flow produces turbulent kinetic energy, i.e., $C(\text{KE}_T, \text{KE}_M) < 0$. Equation (17) is the generation of turbulent kinetic energy from turbulent potential energy by perturbation vertical density fluxes. This is the baroclinic pathway and baroclinic instability occurs when vertical density fluxes restratify the tilted isopycnals, i.e., $C(\text{PE}_T, \text{KE}_T) > 0$. Equations (16) and (17) have units of kg m^2 s^{-3}. A full derivation of these energetic terms can be found in von Storch et al. (2012) and Chen et al. (2014), so we will not cover them here.

d. Potential vorticity

Potential vorticity is used here to diagnose changes in the stability of the anticyclonic eddy from relative wind stress. Following Hoskins et al. (1985), potential vorticity Q is defined as

$$Q = (f + \zeta_g) \partial_z b - (\partial_z v_g)(\partial_x b) + (\partial_z u_g)(\partial_y b), \tag{18}$$

where $b = -g\rho/\rho_0$ is the buoyancy. A necessary condition for the growth of eddy instabilities is the existence of a sign change in radial potential vorticity gradient ($\partial_r Q$) in either the radial or vertical direction (Vallis 2006). When $\partial_r Q$ changes sign in the horizontal it indicates barotropic instabilities, and when the sign of $\partial_r Q$ varies in the vertical, this indicates baroclinic instabilities. In the counterrotating eddy setup, $\partial_r Q$ changes sign in the vertical and it is thus baroclinically unstable (Dewar et al. 1999).

3. Results

a. Wind-induced vertical motions

Normalized relative vorticity ζ_g/f, nonlinear Ekman pumping W_ζ, and vertical velocity w are displayed in Fig. 3 for the absolute wind stress simulation (AW). The W_ζ in this case accounts for total Ekman pumping. These quantities are plotted using daily time-mean model output at day 100 and show the eddy approximately midway through its lifetime. The ζ_g/f maintains a circular symmetric profile with strong anticyclonic vorticity at its center and weak cyclonic vorticity at its periphery (Fig. 3a). The W_ζ displays a dipole pattern of upwelling and downwelling at the eddy center (Fig. 3b), generated through the interaction of constant τ_{abs} and horizontal relative vorticity gradients. The dipole orientation is also dependent on the direction of the wind. The w is shown at a depth of 5 m (Fig. 3c), the first z layer below the surface. The pattern of w is similar to W_ζ in its shape and magnitude. The W_ζ reaches 0.065 m day^{-1} while w exhibits values over 0.1 m day^{-1}. In w, a spiral arm can be seen at the outer edge of each dipole, pointing to a possible growth of azimuthal wavenumber $l = 2$ in the counterrotating eddy setup (Katsman et al. 2003). Plotting w at 5-m depth is done because W_ζ is valid at the base of the Ekman layer. The depth of the Ekman layer is defined using $\delta_E = \sqrt{(2A_z)/f}$ (Vallis 2006) and gives $\delta_E \approx 1.5$ m.

In the relative wind stress simulation (RW), additional quantities are presented in Fig. 4, showing relative wind stress curl $\nabla \times \boldsymbol{\tau}_{\text{rel}}$, linear Ekman pumping W_c, and total Ekman pumping W_{tot}. At day 100, an eddy weakening can first be observed in RW by looking at the plan views of ζ_g/f (Figs. 3a and 4a). Anticyclonic vorticity in RW is weaker than AW as can be seen by the reduction in contour saturation at the eddy
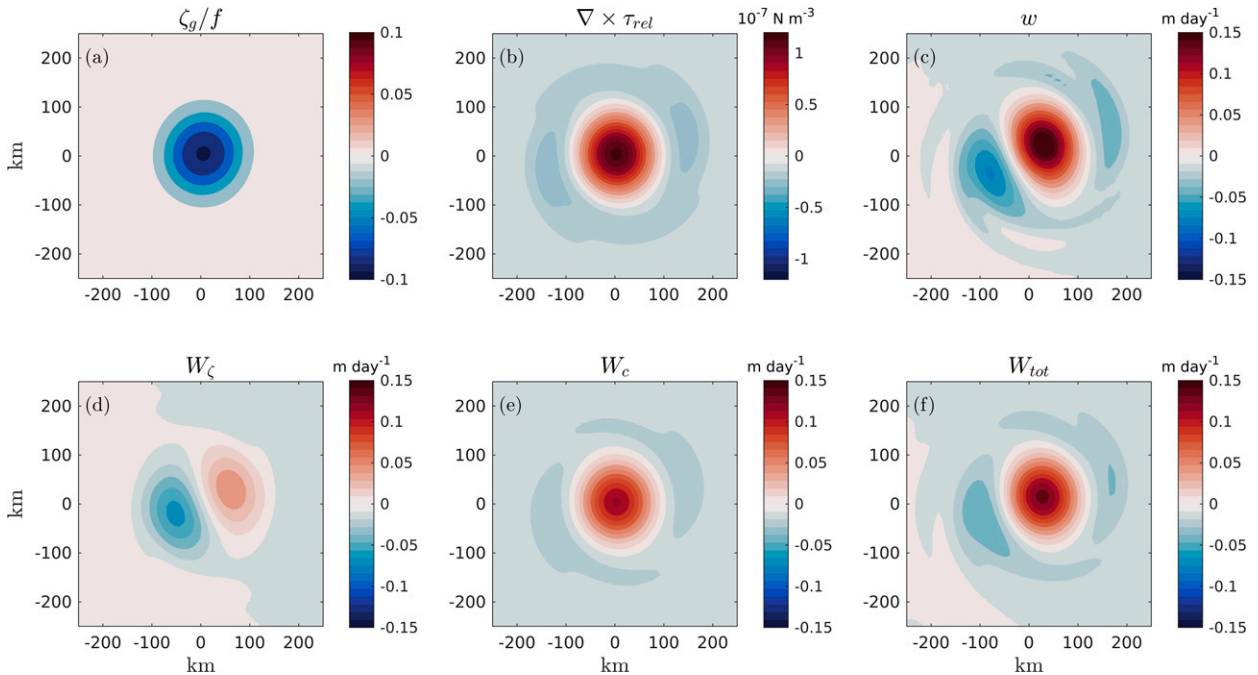
FIG. 4. Horizontal patterns at day 100 in relative wind stress simulation of (a) surface normalized relative vorticity, (b) relative wind stress curl, (c) model output vertical velocity (m day^{-1}) at a depth of 5 m, (d) nonlinear Ekman pumping (m day^{-1}), (e) linear Ekman pumping (m day^{-1}), and (f) total Ekman pumping (m day^{-1}). Quantities are calculated using MITgcm daily time-mean output.

center. This damping of relative vorticity is due to the imposed relative wind stress curl that injects oppositely signed vorticity into the eddy (Fig. 4b). Like AW, RW has a dipole pattern in W_ζ, but more downwelling takes place (Fig. 4d) due to τ_{rel} introducing asymmetry. Additionally, W_ζ is overall weaker than AW, with values around 0.058 m day^{-1}, consistent with the damping of ζ_g/f. The W_c (Fig. 4e) is generated via the wind stress curl, displaying a monopole of upwelling (0.12 m day^{-1}) surrounded by weak downwelling (0.02 m day^{-1}), attenuating the eddy by flattening its isopycnals. The W_{tot} has even stronger central upwelling (0.14 m day^{-1}) and is clearly dominated by the upwelling nature of W_c (Fig. 4f). As with AW, w (Fig. 4c) has similar patterns to W_{tot} but is greater in value as it is deeper than $\delta_E \approx 1.5$ m. Gaube et al. (2015) and Chen et al. (2020) also found similar Ekman pumping patterns to the ones shown here.

Further examination of the eddy vertical velocity field is made in Fig. 5. Away from the eddy surface, horizontal vertical velocity patterns take on a different shape. Figures 5a and 5b show w at day 100 averaged over the top 800 m for absolute and relative wind stress simulations. The w field exhibits alternating up/downwelling cells that encircle the eddy center, which indicate the eddy is not in geostrophic balance (Pilo et al. 2018). The w field is dominated mostly by a four cell pattern, but also exhibits a weaker eight cell pattern toward the periphery. The four cell vertical velocity pattern is similar to the pattern of a linearly unstable vortex with azimuthal wavenumber $l = 2$ seen in Fig. 2 of Dewar et al. (1999), while the eight cell pattern may indicate the existence of higher unstable wavenumbers. Nevertheless, the net effect of relative

wind stress on values of w still remain. The w_{rel} has maximum absolute values up to 0.03 m day^{-1} greater than w_{abs}.

Transects of w show the extension of vertical motions down the water column (Figs. 5c,d). The w_{abs} exhibits a dipole of up/downwelling at the surface, but with depth the modal wave pattern becomes greater than any Ekman pumping effects. Similarly, w_{rel} shows an Ekman pumping pattern at the surface, as seen in Figs. 4c and 4f, but again the modal wave pattern quickly exerts its dominance with depth. The overall increase in w is also visible in Fig. 5e from the surface down to 3000 m. This implies that, although the spatial pattern of w changes with depth, the impact of relative wind stress on vertical velocity remains throughout the water column.

b. Mean eddy energetics

1) DAMPING AND DISSIPATION

The work done by wind on the eddy's geostrophic surface motion at day 100 is shown in Fig. 6. Here, the daily model output is used to calculate wind work at a snapshot in time. Dipoles of positive and negative wind work exist in absolute (Fig. 6a) and relative (Fig. 6b) wind stress simulations. Maximum values of wind work occur in regions of the eddy that have the strongest surface current, which is at the speed-based radius, $L_s \approx 70$ km. In AW, the amount of negative wind work is negated by positive wind work, since there is no current–wind interaction in τ_{abs}, Eq. (2). In RW, in absolute terms, there is around 12% more negative than positive wind work due to the current–wind interaction in τ_{rel}, Eq. (1), seen through the zonal cross section of wind work (Fig. 6c). The
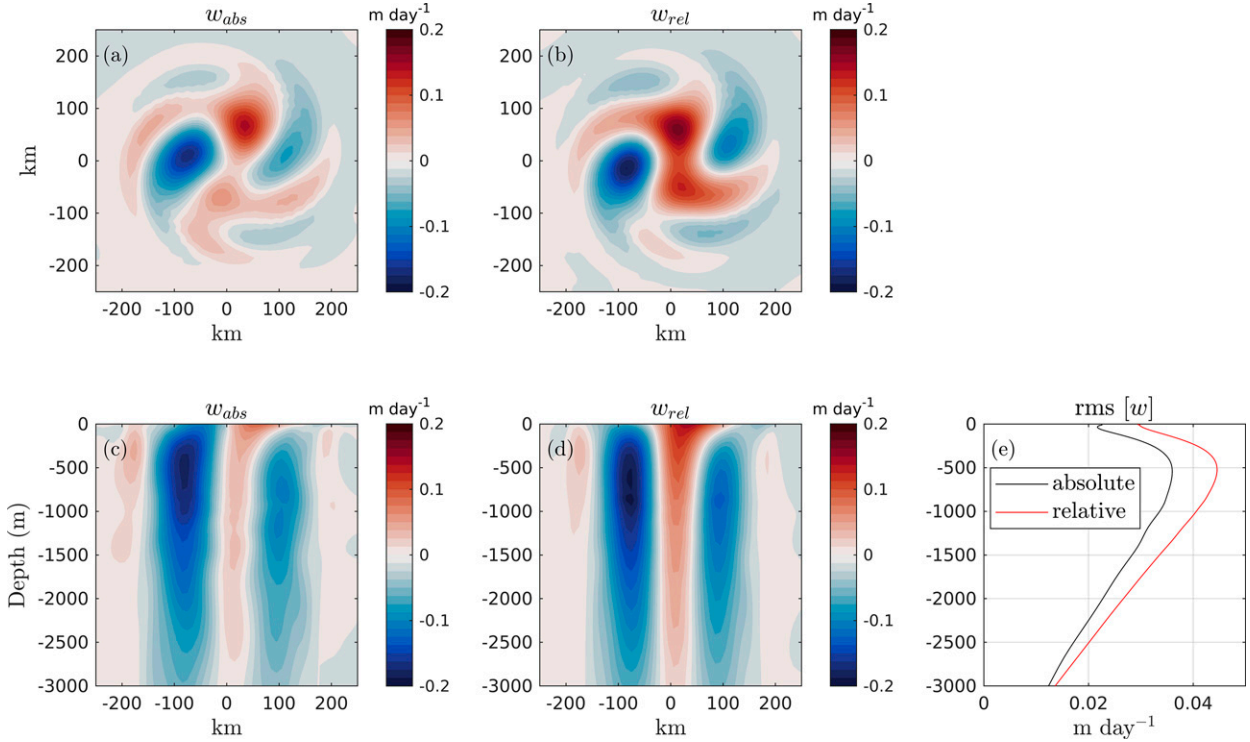
FIG. 5. Model vertical velocity output at day 100 (m day^{-1}). Horizontal patterns averaged over top 800 m for (a) absolute wind stress and (b) relative wind stress, and zonal transects through eddy center for (c) absolute wind stress and (d) relative wind stress. (e) The root-mean-square of vertical velocity for absolute (black) and relative (red) wind stress simulations. Quantities are calculated using MITgcm daily time-mean output.

total wind power input by relative wind stress is seen over time in Fig. 7c and highlights the amount of power being removed from the anticyclonic eddy.

The time evolution of domain integrated mean eddy energetics is shown in Fig. 7. Total eddy energy (KE_M + PE_M) is dominated by PE_M, where KE_M is around an order of magnitude smaller for the first 150 days of the time series (Figs. 7a,b). Dissipation of total energy in RW is larger than AW as a result of work done by relative wind stress (Figs. 6b and 7c), as shown by the more rapid decrease of KE_M + PE_M.

The overall damping of total energy likely reflects a release of PE_M, for which relative wind stress is the most efficient at fulfilling, achieving an additional 7×10^{14} J of dissipation at day 200. Although the wind power input by relative wind stress is negative (Fig. 7c) and consistent with the decay of total eddy energy, it does not explain in full how PE_M is reduced.

From Eq. (12) there are two important terms that govern mean kinetic energy: $C(PE_M, KE_M)$ and P. The P_{rel} in this case is negative (Fig. 7c) and therefore extracts KE_M from the eddy. The exponential growth seen in P_{rel} is associated with the
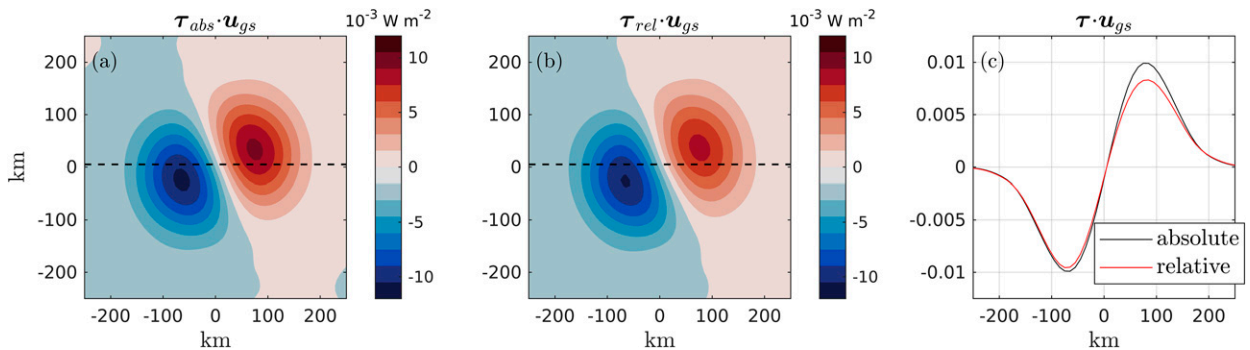

FIG. 6. Horizontal patterns at day 100 of wind work done on the eddy's geostrophic motion (10^{-3} W m^{-2}), for (a) absolute wind stress and (b) relative wind stress simulations. (c) Zonal cross sections—dashed lines in (a) and (b)—of wind work in absolute (black line) and relative (red line) wind stress simulations. Quantities are calculated using MITgcm daily time-mean output.
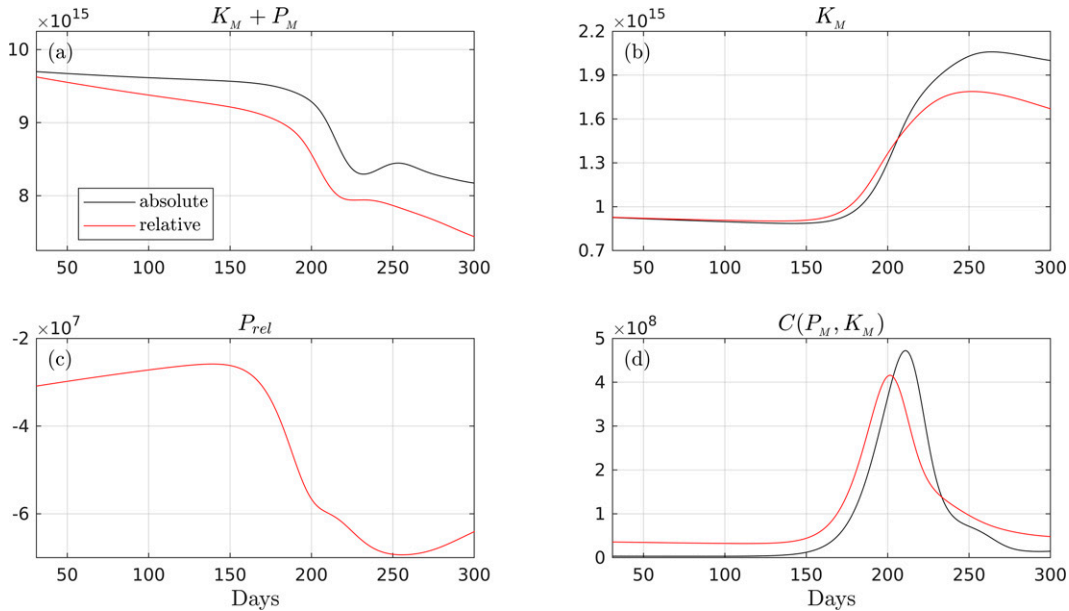
FIG. 7. Time series from day 31 to 300 comparing absolute (black) and relative (red) wind stress simulations of (a) total mean energy, (b) mean kinetic energy, (c) relative wind stress damping, and (d) conversion of mean potential to mean kinetic energy. Terms in (a), (b), and (d) are volume integrals, and (c) is a spatial integral. Each day represents a 16-day time mean. Units of energy in joules and damping/conversion in watts.

exponential growth in KE_M (Fig. 7b) as P_{rel} depends on the ocean surface current speed. The $C(PE_M, KE_M)$ is positive for all time in each simulation (Fig. 7d) and implies PE_M is converted to KE_M. In RW, $C(PE_M, KE_M)$ is greater for most of time and undergoes an earlier exponential growth and decay. The growth of $C(PE_M, KE_M)$ in part explains the increased reduction in total energy (Fig. 7a) since PE_M has to be converted into KE_M before being mechanically dissipated by P_{rel}, or other viscous processes. However, the growth and decay of KE_M in each simulation (Fig. 7b) appears to be governed by $C(PE_M, KE_M)$, even in RW with P_{rel}. Taking a closer look at values of $C(PE_M, KE_M)$ and P_{rel} in Figs. 7c and 7d. At day 31 in the time series, $C(PE_M, KE_M)$ is $\sim 3.4 \times 10^6$ W in AW and 3.6×10^7 W in RW, while P_{rel} in RW is $\sim -3.1 \times 10^7$ W. Additional $C(PE_M, KE_M)$ in RW counteracts P_{rel} by $\sim -1.5 \times 10^6$ W, and by day 100, this has grown to $\sim 2 \times 10^6$ W. This counteracting process by relative wind stress–induced $C(PE_M, KE_M)$ continues until the exponential growth in RW begins to die down.

The effect of relative wind stress on mean kinetic energy and baroclinic conversion is further explored by decomposing their volume contributions into upper and lower layers (Fig. 8). The upper layer is calculated using all z levels above and including 800 m, and the lower layer represents that below. As expected, relative wind stress damps upper mean kinetic energy by around 20% from day 31 up until its exponential growth near to day 150 (Fig. 8a). This damping of surface mean kinetic energy is similar to findings by Seo et al. (2016) and Oerder et al. (2018). It is also clear from this exponential growth in upper-layer KE_M why P_{rel} grows (Fig. 7c). In contrast, lower mean kinetic energy has increased by 3% over the same period as a result of relative wind stress (Fig. 8b). It can

be seen that relative wind stress produces more baroclinic conversion in both layers, showing a deep reaching effect from this surface drag (Figs. 8c,d). In each case, the additional baroclinic conversion is consistent with the larger rms[w] in RW (Fig. 5e). It therefore appears that additional lower-layer baroclinic conversion helps to offset any surface damping.

2) A SCALING ARGUMENT

To provide insight into why additional production of KE_M in RW appears to offset wind damping by relative wind stress, we seek a scaling between $C(PE_M, KE_M)$ and P_{rel}. To account for deviations in density caused by the eddy, $\bar{\rho}$ needs to be replaced in Eq. (13). Using von Storch et al. (2012),

$$\int_V \bar{\rho}\,\overline{w}\,dV = \int_V (\bar{\rho} - \rho_{ref})\overline{w}\,dV = \int_V \overline{\rho^*}\,\overline{w}\,dV. \quad (19)$$

This is true because $\int_V \rho_{ref}\overline{w}\,dV = 0$ as the volume integral of $\overline{w}$ will be zero with no-normal flow boundary conditions. Therefore, $\overline{\rho^*}$ replaces $\bar{\rho}$ in Eq. (13) for this scaling analysis.

Next, additional vertical velocities are generated by relative wind stress–induced Ekman pumping, and it is known that linear Ekman pumping attenuates eddies (Dewar and Flierl 1987; Gaube et al. 2015). We note that a no-wind experiment (not shown) has similar mean energetics to AW, revealing that W_ζ has little effect on $C(PE_M, KE_M)$. Therefore, W_ζ is neglected from this scaling, and $\overline{w}$ is replaced by W_c in Eq. (13), thus

$$C(PE_M, KE_M) = -Hg\overline{\rho^*}\,W_c L_e^2, \quad (20)$$

where L_e is an eddy length scale. To complete this scaling we now need expressions for relative wind stress, wind
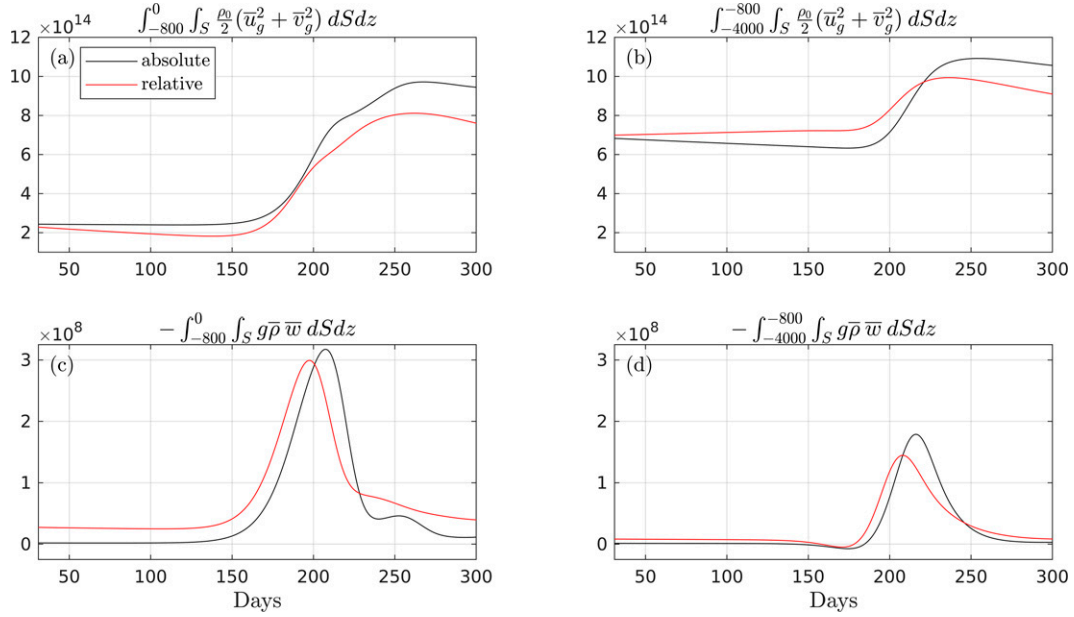
FIG. 8. Time series from day 31 to 300 comparing absolute (black) and relative (red) wind stress simulations of (a) upper-layer mean kinetic energy, (b) lower-layer mean kinetic energy, (c) upper-layer conversion of mean potential to mean kinetic energy, and (d) lower-layer conversion of mean potential to mean kinetic energy. Terms are volume integrated over upper (from 0 to −800 m) and lower (from −800 to −4000 m) layers. Each day represents a 16-day time mean. Units of energy in joules and conversion in watts.

power input by relative wind stress, and linear Ekman pumping.

Following Duhaut and Straub (2006), we find τ_{diff} and P_{diff} that equate to relative minus absolute components. In each case, these will provide the contributions that come entirely from eddy–wind interaction. So, P_{diff} is essentially the amount of energy relative wind stress will take out, meaning $P_{\text{diff}} \sim P_{\text{rel}}$. To find τ_{diff}, it is assumed that only winds aligned with the eddy current contribute to the wind speed magnitude

$$|\mathbf{u}_a - \mathbf{u}_{\text{gs}}| \approx |\mathbf{u}_a| - \mathbf{u}_{\text{gs}} \cdot \mathbf{i} \tag{21}$$

where $\mathbf{i}$ is a unit vector that points in the direction of $\mathbf{u}_a$. Using this assumption, along with Eqs. (1) and (2),

$$\boldsymbol{\tau}_{\text{diff}} \equiv \boldsymbol{\tau}_{\text{rel}} - \boldsymbol{\tau}_{\text{abs}} \approx \rho_a C_d [-|\mathbf{u}_a|\mathbf{u}_{\text{gs}} - (\mathbf{u}_{\text{gs}} \cdot \mathbf{i})\mathbf{u}_a]$$
$$\approx -2\rho_a C_d \mathbf{u}_a \mathbf{u}_{\text{gs}}, \tag{22}$$

where quadratic terms have been neglected, and $\mathbf{u}_a > 0$. Similarly,

$$P_{\text{diff}} \equiv \int_S \boldsymbol{\tau}_{\text{diff}} \cdot \mathbf{u}_{\text{gs}} \, dS \approx -2\rho_a C_d \mathbf{u}_a \mathbf{u}_{\text{gs}}^2 L_e^2. \tag{23}$$

Now, substituting Eq. (22) into Eq. (9) and neglecting the nonlinear component W_ζ gives

$$\hat{W}_c = \frac{\nabla \times \boldsymbol{\tau}_{\text{diff}}}{\rho_0 (f + \zeta_g)} \approx -\frac{2\rho_a C_d \mathbf{u}_a}{\rho_0 f} \zeta_g, \tag{24}$$

where $\hat{W}_c$ neglects the vorticity in the denominator, since $\zeta_g \ll f$. Equation (24) implies that $\hat{W}_c$ generates upwelling

(downwelling) in anticyclonic (cyclonic) regions. Finally, taking Eqs. (20), (23), and (24), and assembling the scaling gives

$$\frac{C(\text{PE}_M, \text{KE}_M)}{P_{\text{rel}}} \sim \frac{Hg\overline{\rho^*}\zeta_g}{\rho_0 f \mathbf{u}_{\text{gs}}^2}. \tag{25}$$

Based on parameters in the anticyclonic eddy, we put $\overline{\rho^*}/\rho_0 \sim 10^{-4}$, $\zeta_g \sim 10^{-6} \text{ s}^{-1}$, $\mathbf{u}_{\text{gs}}^2 \sim 10^{-2} \text{ m}^2 \text{ s}^{-2}$, and values from Table 1 into Eq. (25). These values give a scaling ratio equivalent to 4, showing that additional production of KE_M by W_c offsets damping by relative wind stress. This also supports our numerical findings found in section 3b(1).

c. Destabilization of the eddy

The destabilization of the eddy is first examined using volume integrated turbulent eddy energetics, shown in Fig. 9. Initially, little growth is observed in all terms, consistent with the stable time evolution of KE_M and $C(\text{PE}_M, \text{KE}_M)$ (Figs. 7b,d). Around day 175, growth in terms begin, indicating the start of eddy instabilities. The dominant instability is baroclinic, with $C(\text{PE}_T, \text{KE}_T) > 0$ supplying KE_T (Figs. 9a,b). The barotropic pathway $C(\text{KE}_T, \text{KE}_M)$ is equivalent in magnitude to the baroclinic one, though fluxes of momentum are predominantly directed upgradient, i.e., KE_T is converted to KE_M (Fig. 9c). The vertical shear component of $C(\text{KE}_T, \text{KE}_M)$ is negligible. Indeed, Katsman et al. (2003) found the dominant instability to be baroclinic in a counterrotating eddy regime. It can also be seen that the turbulent peaks all take place shortly after (~10 days) the mean energetic peaks (Figs. 7b,d), indicating that instabilities are prevalent during the eddy's decay stage.
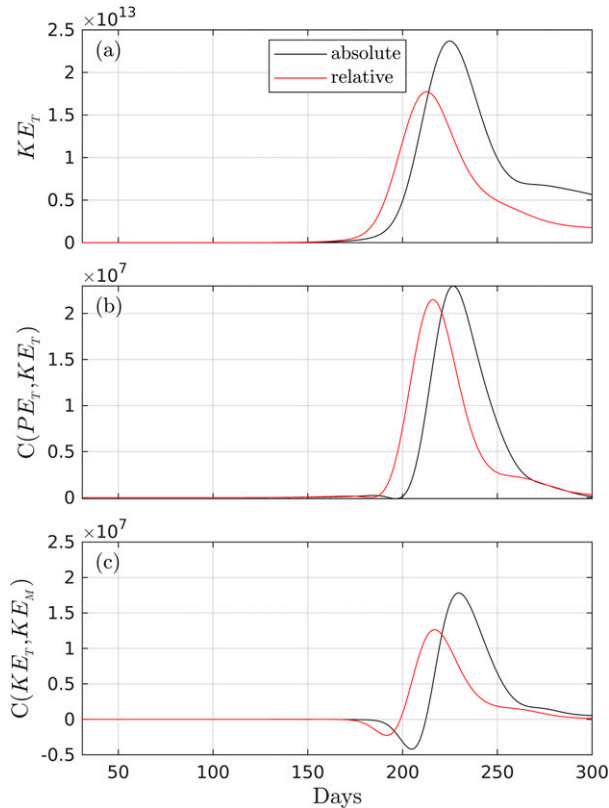
FIG. 9. Time series from day 31 to day 300 comparing absolute (black) and relative (red) wind stress simulations of (a) turbulent kinetic energy, (b) baroclinic pathway, and (c) barotropic pathway. Terms are volume integrated and each day represents a 16-day time mean. Units of energy in joules and instability pathways in watts.

A few differences between wind stress simulations exist. The first one is the time of growth, where RW undergoes its amplification ~10 days earlier. Second, although RW becomes unstable sooner, AW exhibits greater maximum peaks for all quantities, in particular, KE_T is ~30% larger than RW. This implies that relative wind stress initiates instabilities sooner but also damps their overall magnitude. Furthermore, growth across all terms comes from the upper 800 m, with turbulent energetic values in the lower layer at least an order of magnitude smaller (not shown). This is consistent with the eddy's primarily surface intensified nature.

A reason for this earlier instability onset can be attributed to changes in the eddy's PV gradient between the upper and lower layers, shown in Fig. 10 for quantities at day 100. It can be seen through cross sections of PV gradients at the eddy surface that values in RW near to a radius of 50 km increase by factors of 4–8 in response to relative wind stress (Fig. 10c). This increase in PV gradient may be the cause of an earlier onset of baroclinic instability in the eddy (Fig. 9b). Modifications to the surface PV gradient can be seen by considering the contributions to PV in Eq. (18). The dominant component of PV is $(f + \zeta_g)\partial_z b$, and we know that $\zeta_g \ll f$. A cross section of $f\partial_z b$ at the surface (Fig. 10b) is shown to match PV (Fig. 10a), displaying a similar increase in value in RW. The cross sections

at 2000 m depth (Figs. 10e–g) are smaller than the surface quantities and do not vary between wind stress simulations, likely due to $\zeta_g \ll f$ and weak lower-layer stratification (see Fig. 2a). We explain the increase in $f\partial_z b$ through surface buoyancy anomalies at day 100 (Figs. 10d,h). Through the action of linear Ekman pumping, it can be seen in RW that buoyancy is lost (gained) at the eddy center (periphery) through upwelling (downwelling). The Ekman pumping process flattens isopycnals, and by doing so converts horizontal density gradients into vertical density gradients, thus increasing $f\partial_z b$ at the surface. This leads to larger PV and PV gradients at the surface in RW, as well as the earlier growth in turbulent energetics (Fig. 9).

Horizontal plan views of surface ζ_g/f, and turbulent kinetic energy, baroclinic pathway, and barotropic pathway averaged over the top 800 m at day 200 are presented in Fig. 11. Again, ζ_g/f uses daily mean model output, and energetic terms use a 16-day time-mean at day 200. The choice of day 200 is used to illustrate the spatial inhomogeneity of these perturbations prior to the eddy's breakup in each wind stress simulation. In AW, ζ_g/f (Fig. 11a) displays two spiral arms at the north and south side of the eddy, a feature that was first observed and noted in section 3b through Ekman pumping patterns. There is a clear elliptical tripole vorticity pattern with anticyclonic vorticity at the center, much different to the circular profile at day 100 (Fig. 3a). In general, this elliptical pattern is found to be typical of an unstable azimuthal wavenumber $l = 2$ in a baroclinic eddy (Baey and Carton 2002). Turbulent kinetic energy and positive baroclinic pathway are concentrated at each spiral arm and between patches of opposing ζ_g/f near the eddy center, highlighting the instability present in the eddy (Figs. 11b,c). Values in the barotropic pathway are similar to the baroclinic one, but show a tendency for barotropic instability (Fig. 11d), which is also seen through the volume integrated terms in Fig. 9c. In RW, each quantity (Figs. 11e–h) displays a slowdown in azimuthal rotation in response to the damping of upper-layer mean kinetic energy (Fig. 8a). The ζ_g/f profile has become narrower and the stronger north–south anticyclonic regions have initiated their detachment at the origin. Moreover, turbulent kinetic energy and the baroclinic and barotropic pathways are all much stronger than AW, supporting an earlier destabilization, and ultimate breakup, due to relative wind stress.

4. Summary and discussion

Results from this paper highlight the dynamical response of an anticyclonic baroclinic eddy when forced by an absolute or relative wind stress. Rather than examining an eddy through its entire life cycle (i.e., generation to dissipation), a geostrophically balanced eddy was initialized in a mesoscale resolving numerical model to enable the investigation of its spindown process. The relevant mechanisms involved in the decay of this eddy include its vertical velocity, energetics, and potential vorticity. These processes were examined to help answer the questions posed toward the end of the introduction.

(i) *Can relative wind stress lead to a complete eddy spindown?* In this counterrotating eddy setup, relative wind stress dissipates combined mean potential and mean
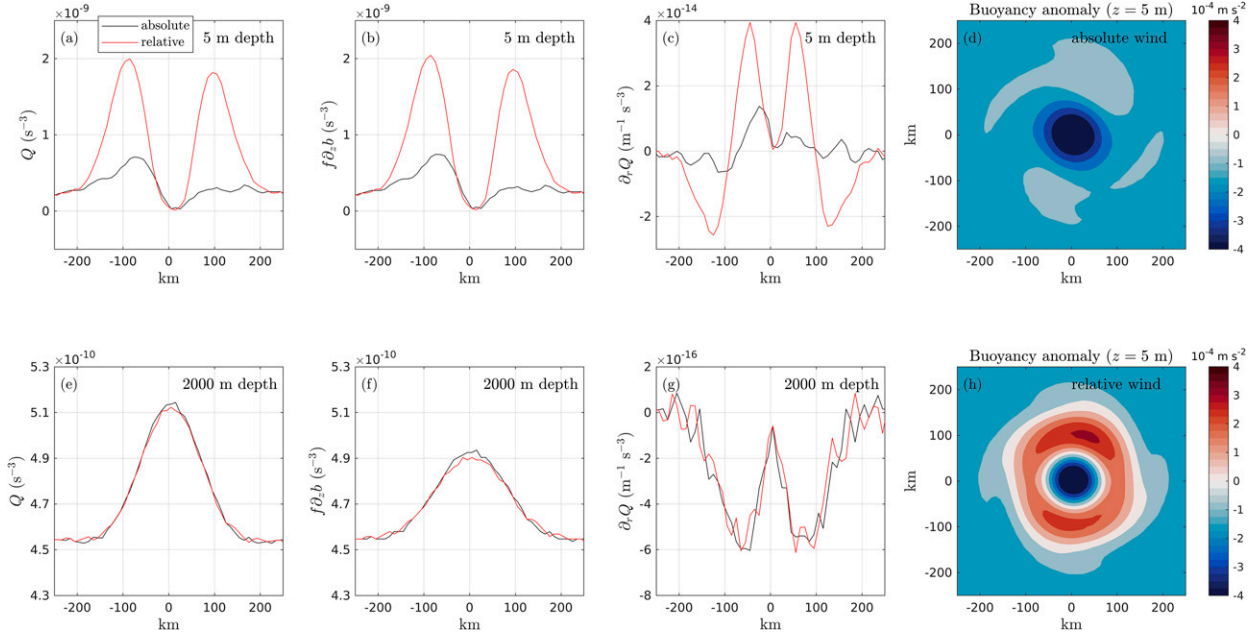
FIG. 10. Meridional cross sections at day 100 at the surface (5 m) and middepth (2000 m) of (a),(e) potential vorticity (10^{-9} s^{-3}), (b),(f) potential vorticity contribution by vertical buoyancy gradient (10^{-9} s^{-3}), and (c),(g) radial potential vorticity gradient (10^{-14} m^{-1} s^{-3}), comparing absolute (black) and relative (red) wind stress simulations. Horizontal plan views of buoyancy anomaly $b(\text{day} = 100) - b(\text{day} = 1)$ (10^{-4} m s^{-2}), at surface (5 m) for (d) absolute and (h) relative wind stress simulations. Quantities are calculated using MITgcm daily time-mean output.

kinetic energy throughout the simulation, consistent with the notion that relative wind stress is a drag mechanism (Dewar and Flierl 1987). However, damping of mean kinetic energy by relative wind stress is offset by an additional production of mean kinetic energy via baroclinic conversion. Moreover, examining upper- and lower-layer mean energetics reveals that relative wind stress damps (energizes) upper-layer (lower-layer) mean kinetic energy. These findings inform us that relative wind stress is more than just a dissipative process,
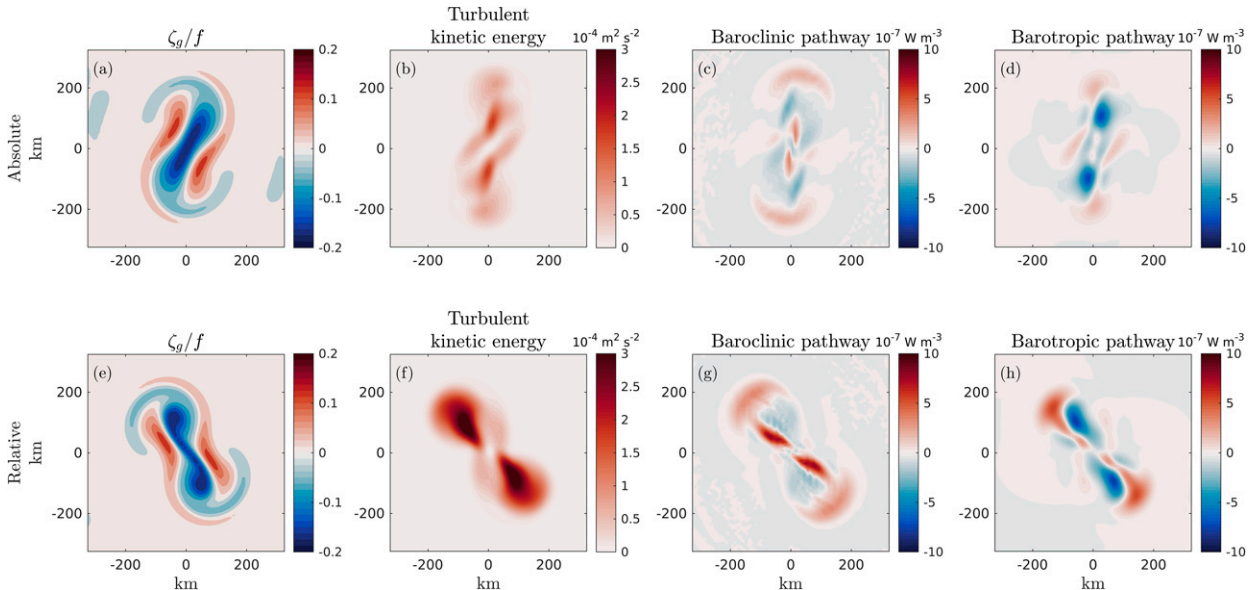

FIG. 11. Horizontal patterns at day 200 of (a),(e) surface normalized relative vorticity, then profiles averaged over top 800 m of (b),(f) $(1/2)\overline{(u_g'^2 + v_g'^2)}$ (10^{-4} m^2 s^{-2}); (c),(g) $-g\overline{\rho'w'}$ (10^{-7} W m^{-3}); and (d),(h) $\rho_0 \overline{u_g'\mathbf{u}'} \cdot \nabla \overline{u}_g + \rho_0 \overline{v_g'\mathbf{u}'} \cdot \nabla \overline{v}_g$ (10^{-7} W m^{-3}). (top) Absolute wind stress and (bottom) relative wind stress. Relative vorticity is calculated using MITgcm daily time-mean output, and energetic terms are 16 day time-means taken at day 200.

enabling a transfer of mean potential to mean kinetic energy and modulation of the eddy spindown process.

(ii) *Can Ekman pumping generate additional baroclinic conversion that offsets relative wind stress damping?* The enhanced production of mean kinetic energy by relative wind stress–induced baroclinic conversion is related to the intensified vertical motions. Relative wind stress imposes a curl over the eddy that generates additional vertical velocities throughout the water column via linear Ekman pumping. These additional vertical motions enable an enhanced transfer of mean potential to mean kinetic energy, capable of counteracting relative wind stress damping. This is made clear with the scaling $C(\text{PE}_M, \text{KE}_M)/P_{\text{rel}} > 1$, implying that relative wind stress–induced baroclinic conversion counteracts relative wind stress damping. This shows that Ekman pumping is an important mechanism for kinetic energy supply (Renault et al. 2018), particularly for the deep eddy flow. Studies have shown little difference in large-scale ocean transport or residual meridional overturning circulation between absolute and relative wind stress (Munday and Zhai 2015; Munday et al. 2021), so it remains unclear what effects an energized deep eddy flow may have. Nevertheless, despite the increase in vertical velocity by relative wind stress, horizontal patterns in each simulation display significant qualitative differences between the surface and at depth. At the surface, Ekman pumping dominates, while at depth, alternating patterns of up/downwelling exist.

(iii) *How might the stability of a baroclinic counter-rotating eddy be affected by relative wind stress?* A further key finding of this study reveals that relative wind stress can modify the stability properties of mesoscale eddies. Because opposing potential vorticity gradients in the upper and lower layer stipulate that a counterrotating eddy will become unstable (Dewar et al. 1999), we demonstrate that an increase in PV gradients at the surface to be the reason for an earlier onset of instability and resulting decay seen in the relative wind stress simulation. The mechanism for these enhanced PV gradients is caused by a conversion of horizontal density gradients into vertical gradients via linear Ekman pumping. In line with findings by Katsman et al. (2003) for counterrotating eddies, the most unstable perturbation comes in the form of baroclinic instability, which we find to occur on a shorter time scale in the relative wind stress simulation due to larger surface PV gradients.

Overall, these results clearly show the response of an anticyclonic eddy to relative wind stress forcing. However, different model setups and eddies could lead to other outcomes. Sutyrin (2016) found for an anticyclonic eddy that adding a middle layer of uniform potential vorticity reduced the growth of eddy instabilities, hence putting forward a way that eddy lifetime can be prolonged. Arbic and Scott (2008) showed quadratic bottom drag to damp bottom layer kinetic energy, and could therefore play a role in the stabilization of mesoscale eddies (Dewar et al. 1999). A cyclonic eddy also plays an essential role in the ocean (e.g., Chenillat et al. 2015), yet one has not been examined here. We expect an eddy–wind interaction to produce a similar dynamical response in a cyclonic eddy as it does in the anticyclonic eddy. That is, relative wind stress will damp surface mean kinetic energy and also modify surface potential vorticity gradients. It is not clear how relative wind stress would develop any additional responses not seen in the anticyclonic eddy. Yet, an asymmetry in the growth rate of unstable wavenumbers between cyclonic and anticyclonic eddies does exist (Katsman et al. 2003; Mahdinia et al. 2017), and so it could be worth exploring whether relative wind stress impacts this.

In this numerical model setup, horizontal grid spacing of $\Delta x, y = 10$ km is employed, in part to keep the model computationally inexpensive, but also capable of fully resolving mesoscale processes. The literature surrounding submesoscale resolving numerical models [$O(1)$ km] is very much in the limelight at this moment in time (Brannigan et al. 2017; Su et al. 2018; Schubert et al. 2020), and it could be argued a study such as this should be employing as high a resolution as possible. Yet, the lack of any substantial work on idealized mesoscale eddy–wind interaction still persists, and it is therefore critical to understand this because of the ubiquity and importance of mesoscale eddies in the world's ocean. We do, however, acknowledge some possible shortcomings of these results due to this mesoscale resolution. It was found in previous work that when horizontal resolution is reduced, a marked increase in vertical motions and surface kinetic energy occur (Lévy et al. 2001). Because of the horizontal resolution used, the mesoscale eddy studied here could have underrepresented energetics that may have repercussions on lifetime and stability. Yet, coupled with the knowledge of how eddies evolve (e.g., Ikeda 1981; Dewar et al. 1999), we expect relative wind stress would still generate a similar outcome at a finer resolution, e.g., $\Delta x, y = 2$ km.

This study demonstrates a complex interaction between surface winds and a baroclinic anticyclonic eddy in an idealized setting. Much of the individual results over the eddy's lifetime are well understood, and therefore robust. Yet, bringing them together in this study has resulted in a novel finding, whereby relative wind stress, thought to be completely dissipative, in fact may energize the eddy mean flow and reduce eddy stability. Therefore, this advances our understanding of mesoscale air–sea interactions, though future work should focus on added complexity in model design.

Data availability statement. Scripts to initialize and post-process the MITgcm data are available at https://github.com/thomaswilder/jpo_eddy-scripts.

REFERENCES

Arbic, B. K., and R. B. Scott, 2008: On quadratic bottom drag, geostrophic turbulence, and oceanic mesoscale eddies. *J. Phys. Oceanogr.*, **38**, 84–103, https://doi.org/10.1175/2007JPO3653.1.

Baey, J.-M., and X. Carton, 2002: Vortex multipoles in two-layer rotating shallow-water flows. *J. Fluid Mech.*, **460**, 151–175, https://doi.org/10.1017/S0022112002008170.

Brannigan, L., D. P. Marshall, A. C. N. Garabato, A. J. G. Nurser, and J. Kaiser, 2017: Submesoscale instabilities in mesoscale eddies. *J. Phys. Oceanogr.*, **47**, 3061–3085, https://doi.org/10.1175/JPO-D-16-0178.1.

Chelton, D., M. Schlax, and R. Samelson, 2011: Global observations of nonlinear mesoscale eddies. *Prog. Oceanogr.*, **91**, 167–216, https://doi.org/10.1016/j.pocean.2011.01.002.

Chen, K., P. Gaube, and E. Pallás-Sanz, 2020: On the vertical velocity and nutrient delivery in warm core rings. *J. Phys. Oceanogr.*, **50**, 1557–1582, https://doi.org/10.1175/JPO-D-19-0239.1.

Chen, R., G. R. Flierl, and C. Wunsch, 2014: A description of local and nonlocal eddy-mean flow interaction in a global eddy-permitting state estimate. *J. Phys. Oceanogr.*, **44**, 2336–2352, https://doi.org/10.1175/JPO-D-14-0009.1.

Chenillat, F., P. Franks, P. Rivière, X. Capet, and N. Grima, 2015: Plankton dynamics in a cyclonic eddy in the Southern California Current system. *J. Geophys. Res. Oceans*, **120**, 5566–5588, https://doi.org/10.1002/2015JC010826.

Clément, L., E. Frajka-Williams, K. L. Sheen, J. A. Brearley, and A. C. N. Garabato, 2016: Generation of internal waves by eddies impinging on the western boundary of the North Atlantic. *J. Phys. Oceanogr.*, **46**, 1067–1079, https://doi.org/10.1175/JPO-D-14-0241.1.

Dewar, W. K., and G. Flierl, 1987: Some effects of the wind on rings. *J. Phys. Oceanogr.*, **17**, 1653–1667, https://doi.org/10.1175/1520-0485(1987)017<1653:SEOTWO>2.0.CO;2.

——, and P. D. Killworth, 1995: On the stability of oceanic rings. *J. Phys. Oceanogr.*, **25**, 1467–1487, https://doi.org/10.1175/1520-0485(1995)025<1467:OTSOOR>2.0.CO;2.

——, ——, and J. R. Blundell, 1999: Primitive-equation instability of wide oceanic rings. Part II: Numerical studies of ring stability. *J. Phys. Oceanogr.*, **29**, 1744–1758, https://doi.org/10.1175/1520-0485(1999)029<1744:PEIOWO>2.0.CO;2.

Duhaut, T., and D. Straub, 2006: Wind stress dependence on ocean surface velocity: Implications for mechanical energy input to ocean circulation. *J. Phys. Oceanogr.*, **36**, 202–211, https://doi.org/10.1175/JPO2842.1.

Ferrari, R., and C. Wunsch, 2009: Ocean circulation kinetic energy: Reservoirs, sources, and sinks. *Annu. Rev. Fluid Mech.*, **41**, 253–282, https://doi.org/10.1146/annurev.fluid.40.111406.102139.

Gaube, P., D. B. Chelton, P. G. Strutton, and M. J. Behrenfeld, 2013: Satellite observations of chlorophyll, phytoplankton biomass, and Ekman pumping in nonlinear mesoscale eddies. *J. Geophys. Res. Oceans*, **118**, 6349–6370, https://doi.org/10.1002/2013JC009027.

——, D. McGillicuddy, D. Chelton, M. Behrenfeld, and P. Strutton, 2014: Regional variations in the influence of mesoscale eddies on near-surface chlorophyll. *J. Geophys. Res. Oceans*, **119**, 8195–8220, https://doi.org/10.1002/2014JC010111.

——, D. Chelton, R. Samelson, M. Schlax, and L. O'Neill, 2015: Satellite observations of mesoscale eddy-induced Ekman pumping. *J. Phys. Oceanogr.*, **45**, 104–132, https://doi.org/10.1175/JPO-D-14-0032.1.

Hill, C., D. Ferreira, J.-M. Campin, J. Marshall, R. Abernathey, and N. Barrier, 2012: Controlling spurious diapycnal mixing in eddy-resolving height-coordinate ocean models – Insights from virtual deliberate tracer release experiments. *Ocean Modell.*, **45–46**, 14–26, https://doi.org/10.1016/j.ocemod.2011.12.001.

Hoskins, B. J., M. E. McIntyre, and A. W. Robertson, 1985: On the use and significance of isentropic potential vorticity maps. *Quart. J. Roy. Meteor. Soc.*, **111**, 877–946, https://doi.org/10.1002/qj.49711147002.

Hughes, C., and C. Wilson, 2008: Wind work on the geostrophic ocean circulation: An observational study of the effect of small scales in the wind stress. *J. Geophys. Res.*, **113**, C02016, https://doi.org/10.1029/2007JC004371.

Ikeda, M., 1981: Instability and splitting of mesoscale rings using a two-layer quasi-geostrophic model on an *f*-plane. *J. Phys. Oceanogr.*, **11**, 987–998, https://doi.org/10.1175/1520-0485(1981)011<0987:IASOMR>2.0.CO;2.

Katsman, C., P. Vaart, H. Dijkstra, and W. Ruijter, 2003: Stability of multilayer ocean vortices: A parameter study including realistic Gulf Stream and Agulhas rings. *J. Phys. Oceanogr.*, **33**, 1197–1218, https://doi.org/10.1175/1520-0485(2003)033<1197:SOMOVA>2.0.CO;2.

Lévy, M., P. Klein, and A.-M. Treguier, 2001: Impact of submesoscale physics on production and subduction of phytoplankton in an oligotrophic regime. *J. Mar. Res.*, **59**, 535–565, https://doi.org/10.1357/002224001762842181.

Ma, X., and Coauthors, 2016: Western boundary currents regulated by interaction between ocean eddies and the atmosphere. *Nature*, **535**, 533–537, https://doi.org/10.1038/nature18640.

Mahdinia, M., P. Hassanzadeh, P. Marcus, and C.-H. Jiang, 2017: Stability of three-dimensional Gaussian vortices in an unbounded, rotating, vertically stratified, Boussinesq flow: Linear analysis. *J. Fluid Mech.*, **824**, 97–134, https://doi.org/10.1017/jfm.2017.303.

Marshall, J., A. Adcroft, C. Hill, L. Perelman, and C. Heisey, 1997: A finite-volume, incompressible Navier Stokes model for studies of the ocean on parallel computers. *J. Geophys. Res.*, **102**, 5753–5766, https://doi.org/10.1029/96JC02775.

McClean, J. L., and Coauthors, 2011: A prototype two-decade fully-coupled fine-resolution CCSM simulation. *Ocean Modell.*, **39**, 10–30, https://doi.org/10.1016/j.ocemod.2011.02.011.

McGillicuddy, D., 2015: Formation of intrathermocline lenses by eddy-wind interaction. *J. Phys. Oceanogr.*, **45**, 606–612, https://doi.org/10.1175/JPO-D-14-0221.1.

McGillicuddy, L., and Coauthors, 2007: Eddy/wind interactions stimulate extraordinary mid-ocean plankton blooms. *Science*, **316**, 1021–1026, https://doi.org/10.1126/science.1136256.

Munday, D. R., and X. Zhai, 2015: Sensitivity of Southern Ocean circulation to wind stress changes: Role of relative wind stress. *Ocean Modell.*, **95**, 15–24. https://doi.org/10.1016/j.ocemod.2015.08.004.

——, ——, J. Harle, A. C. Coward, and A. G. Nurser, 2021: Relative vs. absolute wind stress in a circumpolar model of the Southern Ocean. *Ocean Modell.*, **168**, 101891, https://doi.org/10.1016/j.ocemod.2021.101891.

Oerder, V., F. Colas, S. Masson, and F. Lemarié, 2018: Impacts of the mesoscale ocean-atmosphere coupling on the Peru-Chile Ocean dynamics: The current-induced wind stress modulation. *J. Geophys. Res. Oceans*, **123**, 812–833, https://doi.org/10.1002/2017JC013294.

Pacanowski, R., 1987: Effect of equatorial currents on surface stress. *J. Phys. Oceanogr.*, **17**, 833–838, https://doi.org/10.1175/1520-0485(1987)017<0833:EOECOS>2.0.CO;2.

Pierrehumbert, R. T., and K. L. Swanson, 1995: Baroclinic instability. *Annu. Rev. Fluid Mech.*, **27**, 419–467, https://doi.org/10.1146/annurev.fl.27.010195.002223.

Pilo, G. S., P. R. Oke, R. Coleman, T. Rykova, and K. Ridgway, 2018: Patterns of vertical velocity induced by eddy distortion in an ocean model. *J. Geophys. Res. Oceans*, **123**, 2274–2292, https://doi.org/10.1002/2017JC013298.

Prather, M. J., 1986: Numerical advection by conservation of second-order moments. *J. Geophys. Res.*, **91**, 6671–6681, https://doi.org/10.1029/JD091iD06p06671.

Renault, L., M. Jeroen Molemaker, J. Gula, S. Masson, and J. McWilliams, 2016a: Control and stabilization of the Gulf Stream by oceanic current interaction with the atmosphere. *J. Phys. Oceanogr.*, **46**, 3439–3453, https://doi.org/10.1175/JPO-D-16-0115.1.

——, ——, J. McWilliams, A. Shchepetkin, F. Lemairé, D. Chelton, S. Illig, and A. Hall, 2016b: Modulation of wind-work by oceanic current interaction with the atmosphere. *J. Phys. Oceanogr.*, **46**, 1686–1704, https://doi.org/10.1175/JPO-D-15-0232.1.

——, J. McWilliams, and J. Gula, 2018: Dampening of submesoscale currents by air-sea stress coupling in the Californian upwelling system. *Sci. Rep.*, **8**, 13388, https://doi.org/10.1038/s41598-018-31602-3.

Schubert, R., J. Gula, R. J. Greatbatch, B. Baschek, and A. Biastoch, 2020: The submesoscale kinetic energy cascade: Mesoscale absorption of submesoscale mixed layer eddies and frontal downscale fluxes. *J. Phys. Oceanogr.*, **50**, 2573–2589, https://doi.org/10.1175/JPO-D-19-0311.1.

Seo, H., A. J. Miller, and J. R. Norris, 2016: Eddy–wind interaction in the California current system: Dynamics and impacts. *J. Phys. Oceanogr.*, **46**, 439–459, https://doi.org/10.1175/JPO-D-15-0086.1.

Shan, X., Z. Jing, B. Sun, and L. Wu, 2020: Impacts of ocean current–atmosphere interactions on mesoscale eddy energetics in the Kuroshio extension region. *Geosci. Lett.*, **7**, 3, https://doi.org/10.1186/s40562-020-00152-w.

Song, H., J. Marshall, D. J. McGillicuddy Jr., and H. Seo, 2020: Impact of current-wind interaction on vertical processes in the Southern Ocean. *J. Geophys. Res. Oceans*, **125**, e2020JC016046, https://doi.org/10.1029/2020JC016046.

Stern, M. E., 1965: Interaction of a uniform wind stress with a geostrophic vortex. *Deep-Sea Res. Oceanogr. Abstr.*, **12**, 355–367, https://doi.org/10.1016/0011-7471(65)90007-0.

Stewart, K., A. Hogg, S. Griffies, A. Heerdegen, M. Ward, P. Spence, and M. England, 2017: Vertical resolution of baroclinic modes in global ocean models. *Ocean Modell.*, **113**, 50–65, https://doi.org/10.1016/j.ocemod.2017.03.012.

Su, Z., J. Wang, P. Klein, A. Thompson, and D. Menemenlis, 2018: Ocean submesoscales as a key component of the global heat budget. *Nat. Commun.*, **9**, 775, https://doi.org/10.1038/s41467-018-02983-w.

Sutyrin, G. G., 2016: On sharp vorticity gradients in elongating baroclinic eddies and their stabilization with a solid-body rotation. *Geophys. Res. Lett.*, **43**, 5802–5811, https://doi.org/10.1002/2016GL069019.

Thompson, A., K. Heywood, S. Schmidtko, and A. Stewart, 2014: Eddy transport as a key component of the Antarctic overturning circulation. *Nat. Geosci.*, **7**, 879–884, https://doi.org/10.1038/ngeo2289.

Vallis, G. K., 2006: Atmospheric and Oceanic Fluid Dynamics. Cambridge University Press, 745 pp.

von Storch, J.-S., C. Eden, I. Fast, H. Haak, D. Hernandez-Deckers, E. Maier-Reimer, J. Marotzke, and D. Stammer, 2012: An estimate of the Lorenz energy cycle for the world ocean based on the 1/10° STORM/NCEP simulation. *J. Phys. Oceanogr.*, **42**, 2185–2205, https://doi.org/10.1175/JPO-D-12-079.1.

Xu, C., X. Zhai, and X.-D. Shang, 2016: Work done by atmospheric winds on mesoscale ocean eddies. *Geophys. Res. Lett.*, **43**, 12 174–12 180, https://doi.org/10.1002/2016GL071275.

Youngs, M. K., A. F. Thompson, A. Lazar, and K. J. Richards, 2017: ACC meanders, energy transfer, and mixed barotropic–baroclinic instability. *J. Phys. Oceanogr.*, **47**, 1291–1305, https://doi.org/10.1175/JPO-D-16-0160.1.

Zhai, X., and R. Greatbatch, 2007: Wind work in a model of the northwest Atlantic Ocean. *Geophys. Res. Lett.*, **34**, L04606, https://doi.org/10.1029/2006GL028907.

——, H. Johnson, and D. Marshall, 2010: Significant sink of ocean-eddy energy near western boundaries. *Nat. Geosci.*, **3**, 608–612, https://doi.org/10.1038/ngeo943.

——, ——, ——, and C. Wunsch, 2012: On the wind power input to the ocean general circulation. *J. Phys. Oceanogr.*, **42**, 1357–1365, https://doi.org/10.1175/JPO-D-12-09.1.

Zhang, Z., W. Wang, and B. Qiu, 2014: Oceanic mass transport by mesoscale eddies. *Science*, **345**, 322–324, https://doi.org/10.1126/science.1252418.